Welding and Weldability of Nickel-Iron Aluminides

The ductile nickel-iron aluminides can be electron beam welded using a narrow range of welding conditions

BY S. A. DAVID, W. A. JEMIAN, C. T. LIU AND J. A. HORTON

ABSTRACT. An important area in the development of any commercial alloy is the ease with which it may be joined or welded. A study was undertaken to investigate the weldability of the boron-doped (500 ppm by weight) ductile aluminides by gas tungsten arc (GTA) and electron beam (EB) welding processes.

Autogenous GTA welding of boron-containing nickel-iron aluminides produced severe cracking within the weld metal and the heat-affected zone (HAZ). The hot cracking appears to be related to complex phase changes that the material undergoes at elevated temperatures in the HAZ and also during the liquid-to-solid transformation in the fusion zone. A series of EB welds with welding speeds ranging from 13 to 64 mm/s (30 to 150 ipm) with varying beam focus conditions gave successful complete joint penetration welds only in a narrow range of speeds and focus conditions.

The cracks were predominantly intergranular in the HAZ and interdendritic in the fusion zone, presumably associated with the presence of NiAl (β') phase along the grain boundaries and interdendritic regions. Transmission electron microscopy (TEM) revealed tetragonal distortions of the ordered B2 (NiAl type) phase with a martensitic appearance. Microprobe analysis revealed extensive solute redistribution in the fusion zone and the HAZ as a result of the weld thermal cycle.

Paper presented at the 65th AWS Annual Convention held in Dallas, Texas, during April 8-13, 1984.

S. A. DAVID, C. T. LIU and J. A. HORTON are members of the Metals and Ceramics Division, Oak Ridge National Laboratory, Oak Ridge, Tennessee; W. A. JEMIAN is with the Mechanical Engineering and Materials Engineering Department, Auburn University, Auburn, Alabama.

Introduction

Austenitic stainless steels and superalloys are the common heat-resistant materials for structural use at elevated temperatures. The alloys typically contain (15 to 30 wt-%) chromium (Cr) for oxidation and corrosion resistance. The strategic nature of the chromium supply has evoked an increasing interest in development of aluminides as a substitute for chromium-containing alloys.

Nickel (Ni) and iron (Fe) aluminides are in a class of materials usually referred to as intermetallic compounds. The aluminides are generally strong, stable, and resistant to oxidation and corrosion at elevated temperatures (Ref. 1). Unlike conventional alloys, the static strength of many aluminides increases rather than decreases with increasing test temperature (Refs. 2,3). A major problem with using aluminides as structural materials is their reported brittle fracture and low ductility, particularly at lower temperatures (Refs. 2,4). Because of poor fabricability and low fracture toughness, the aluminides have not been considered as serious candidates for structural engineering applications.

Recent studies of microalloying (Refs. 5,6) have demonstrated that additions of a few hundred parts per million of boron dramatically improve the fabricability and ductility of polycrystalline Ni_3Al. By control of boron concentration and thermomechanical treatment, room temperature ductility of 54% has been achieved (Ref. 5). This is the highest tensile ductility ever achieved in polycrystalline aluminides.

An important area in the development of any commercial alloy is the ease with which it may be joined or welded. This paper describes the weldability of this class of alloys and identifies factors controlling the weldability and microstructural features.

Experimental Procedure

Alloys used in this investigation are listed in Table 1. Of these, the alloys of principal interest are aluminides designated IC-25 and IC-14 and were tested in the form of recrystallized sheets. The compositions of these two alloys are identical except for slightly lower aluminum and manganese contents in IC-25. A series of Ni_3Al alloys with varying

Table 1—Alloy Compositions, Wt-%

Alloy	Al	Fe	Mn	Ti	B	Ni
IC-2	12.7					Balance
IC-6	12.7				0.1	Balance
IC-14	10.8	10.7	1.1	0.5	0.05	Balance
IC-15	12.7				0.05	Balance
IC-18	12.7				0.25	Balance
IC-19	12.7				0.01	Balance
IC-25	9.8	10.7	0.5	0.5	0.05	Balance

amounts of boron was also studied to determine the effect of boron on weldability. The aluminides were prepared by arc melting and drop casting alloys from electrolytic iron, pure nickel and aluminum, and a Ni-4% B master alloy.

Although initial weldability studies were carried out with the gas tungsten arc welding process, most of the work reported herein was carried out with the electron beam welding process. Electron beam welds were made on alloy coupons 50 X 50 X 0.7 mm (1.97 X 1.97 X 0.03 in.). Beam voltage and current were adjusted to produce complete penetration welds. A series of autogenous welds (melt runs) was made with systematic variations in travel speed and beam focus. A Hamilton Standard 6 kW electron beam welding machine was used. The welding speed varied from 2 to 64 mm/s (4.7 to 151 ipm). The focus control number was varied 25 digits above sharp focus on the sheet surface.

Various sections of the welds were prepared for metallographic observation by standard techniques. The samples were etched with a solution containing 20 parts HNO_3, 10 parts HF, 20 parts H_3PO_4, and 20 parts H_2O by volume.

Specimens were prepared for transmission electron microscopy (TEM) by spark discharge machining 3 mm (0.12 in.) disks from the welded specimens followed by electropolishing the disks in an electrolyte of 70% ethanol, 10% butyl Cellusolve, 12.5% distilled water, and 7.5% perchloric acid at −10°C (14°F) in a Tenupol electropolishing unit. Transmission electron microscopy examinations were conducted using a Philips EM400T equipped with a field emission gun and an EDAX energy dispersive detector (ED5). Standardless quantification routines of Zaluzec (Ref. 7) were used for data reduction.

Results and Discussion

Phase Diagram and Solidification

Figure 1 shows the binary Al-Ni phase diagram (Ref. 8). Figure 2 depicts a vertical section at 10 wt-% Fe of the Al-Fe-Ni system constructed from projections of the system at various isotherms (Ref. 9). These diagrams show possible sequences of phase separation during solidification for various alloy compositions. However, the solidification behavior and phase separation of weld metal of these alloys may depart considerably from the phase diagrams as a result of trace additions and rapid cooling conditions of the weld metal. Nevertheless, these phase diagrams may be used as a rough guide to indicate the sequences of phase separation that occur during weld pool solidification in these alloys.

The compositions of various alloys of interest are repesented by vertical lines superimposed on the phase diagrams. Phase definitions are the following: γ is disordered fcc, γ' is ordered fcc ($L1_2$), β is the ordered bcc (B2) structure, and β' (not shown on the equilibrium phase diagram but identified in nickel-iron aluminide weldments as a second phase) is a transformed ordered bcc (B2) phase.

For alloy IC-15 represented on Fig. 1,

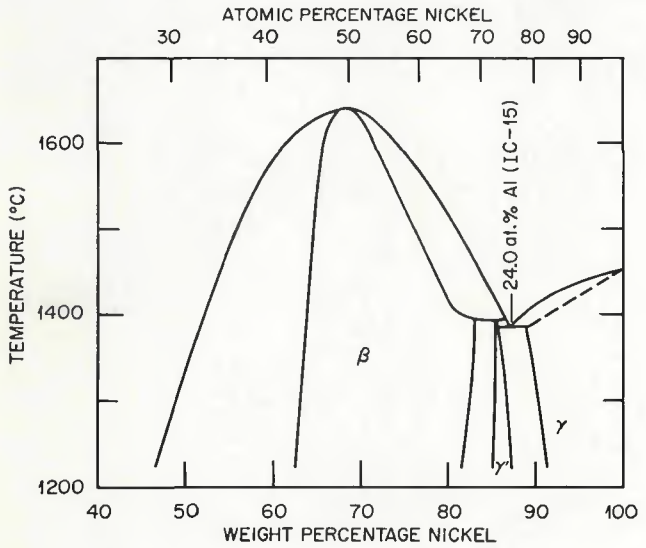

Fig. 1—Binary nickel-iron equilibrium phase diagram, reproduced with permission from ASM (Ref. 8)

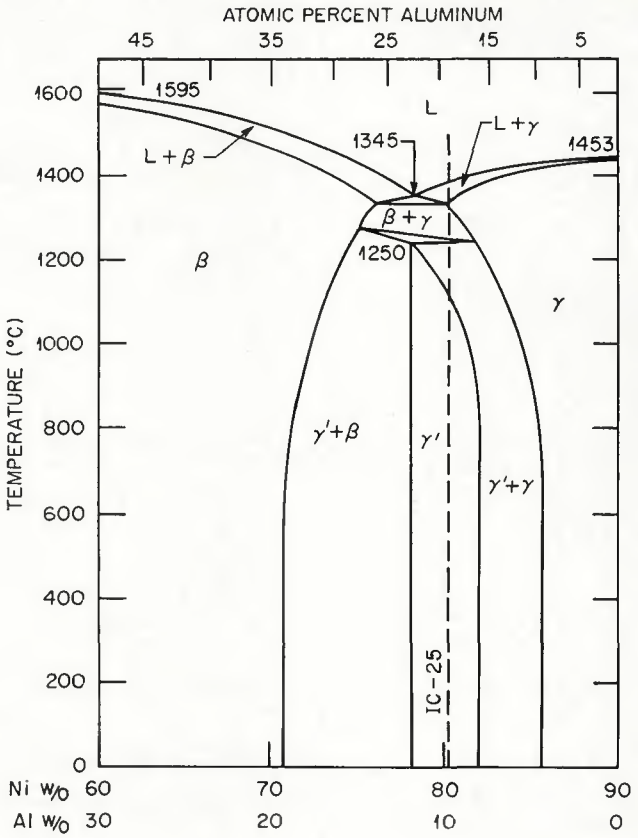

Fig. 2 (right)—Vertical section of the Ni-Al-Fe phase diagram at 10 wt-% Fe. The dashed line represents approximately the composition of IC-25 Ni-Fe aluminide

the primary phase to form from the liquid is γ, with the liquid composition enriching in aluminum until it reaches the eutectic composition. Then the large fraction of the liquid remaining transforms isothermally to $\gamma' + \gamma$ phase mixture. On further cooling the nickel-rich solid solution γ undergoes an ordering reaction leading to the formation of 100% γ'. The addition of trace amounts of boron is believed to have very little effect on the above sequences of events. Even under the nonequilibrium solidification conditions encountered during welding of an alloy of this particular composition, the resulting phase is nearly 100% γ'.

Possible phase fields encountered by an alloy of composition IC-25 during welding are shown in Fig. 2. This has been confirmed by differential thermal analysis and interrupted heating and cooling experiments. During solidification of an alloy of this composition, the primary phase to form from the liquid is γ solid solution with aluminum partitioning to the liquid. As cooling continues, the volume fraction of γ increases, with the aluminum-enriched liquid in the interdendritic region eventually producing β (NiAl), which then transforms to β' (NiAl) because of rapid cooling during welding.

As described previously, the β' phase is a transformed ordered bcc (B2) phase with a martensitic appearance as evidenced by TEM. Addition of iron to the alloy promotes indirectly the formation of β'. As Fe is added to Ni_3Al, it has been found that Fe can occupy both Ni and Al sites in L12 structure of Ni_3Al, thus making more Al available for the formation of β' phase which is mainly NiAl (Ref. 10).

On further cooling, the γ phase undergoes an ordering reaction to γ'. The observed $\gamma' + \beta'$ duplex weld metal microstructure in Fig. 3 also confirms this. Figure 3 also shows a microprobe trace across several secondary dendrite arms. The interdendritic regions are enriched in aluminum, titanium, and manganese and depleted in nickel. The β' is located in the interdendritic region.

Weldability

Effect of Operating Parameters. Initial gas tungsten arc welding (GTAW) of boron-containing nickel-iron aluminide IC-25 revealed severe cracking within the weld metal and the heat-affected zone (HAZ). It is known that the different manifestations of cracking during welding are the following (Refs. 11-14):

1. Solidification cracking,
2. Liquation cracking in the HAZ,
3. Combination of the above two, and
4. Elevated temperature (subsolidus) cracking during heat treatment of welds.

Weld cracking due to the above factors has been the subject of a number of experimental studies (Refs. 11-15). In IC-25 the cracking appears to initiate in the HAZ and sometimes propagate into the fusion zone. A similar problem was encountered in thorium-doped iridium alloys used in radioisotopic thermoelectric generators for space applications; this problem was attributed to the formation of liquation cracks in the HAZ and further propagation of these cracks into the fusion zone (Ref. 15). However, careful examination of the cracked surfaces in IC-25 revealed no evidence of liquation cracking. Also, the cracking problem during GTA welding of iridium alloys was in part due to the nature of the heat source available in the GTA process (Ref. 15).

In iridium alloys, the cracking problem was overcome by electron beam (EB) or laser beam welding processes with their highly concentrated heat source capability. Also, the EB as a heat source can be controlled more precisely than can an electric arc. Hence, autogenous EB welds were made at various welding speeds and focus conditions. Spiking observed normally under sharp focus conditions during EB welding of thin sheet material was never observed during welding of this alloy.

The results are summarized in Fig. 4. Most of the welds showed microcracks in the fusion zone and in the HAZ. However, successful complete penetration welds were made in a narrow range of welding speeds and focus conditions D_f (D_f is the focus number defined as the

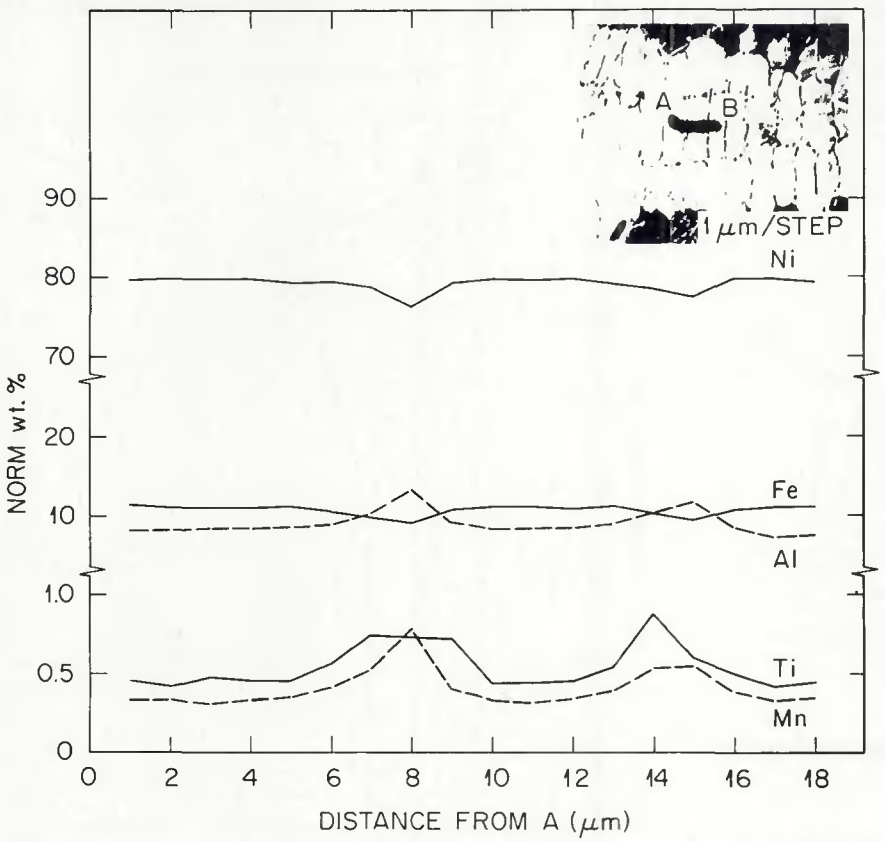

Fig. 3—Microprobe trace across a few secondary dendrite arms in the fusion zone of the weldment

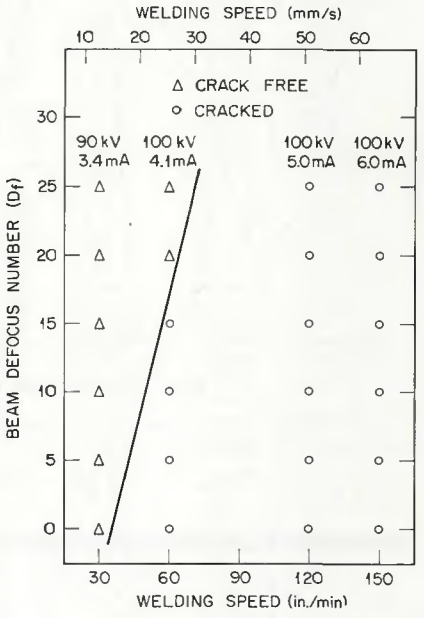

Fig. 4—Weldability of Ni-Fe aluminide as a function of electron beam focus condition and travel speed

difference between the sharp focus number and the focus number used for welding).

Figure 4 shows the operating conditions for welds with and without cracking. Also, the cracking severity has been found to be a strong function of welding speed, as shown in Fig. 5. Cracking severity in this investigation is defined as the number of microcracks per unit length of the weld as observed on the weld surface. The cracking severity of the alloy increases dramatically at welding speeds greater than 12.7 mm/s (30 ipm). The same trend is evident in Fig. 4 as well.

The observed increase in cracking severity at high welding speeds may be attributed to the high heating and cooling rates and associated steep thermal stress gradients that develop within the fusion and HAZ. These factors may contribute to localization of stress that may exceed high temperature fracture strength. Possible loss of ductility at elevated temperatures may add another dimension to the observed cracking problem during welding.

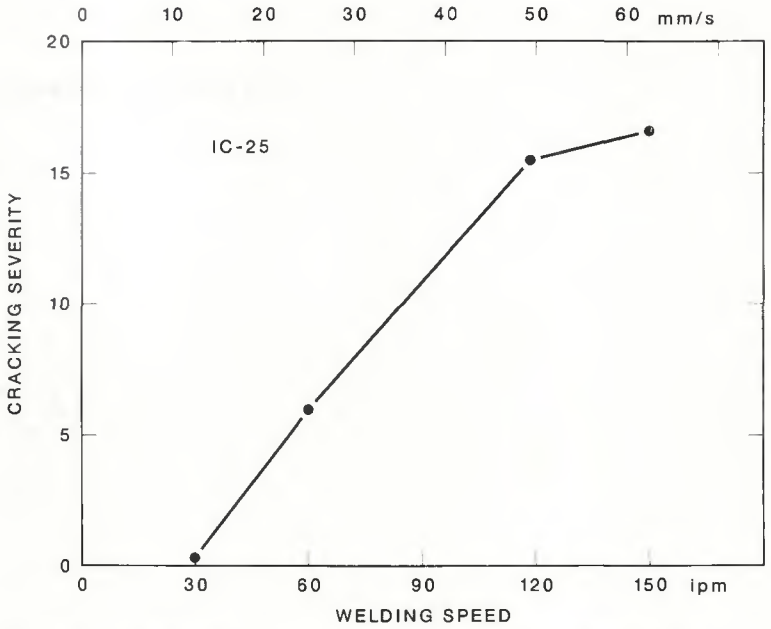

Fig. 5—Weld cracking sensitivity of Ni-Fe aluminide as a function of welding speed

Effect of Boron. Problems related to weldability—in particular, cracking—have traditionally been associated with unwanted, difficult-to-eliminate tramp elements, such as phosphorus and sulfur, in both the base and filler metals. However, it is also true that intentional minor alloy additions also affect weldability, as in the case of carbon and boron in nickel-base superalloys (Ref. 16). Although boron has been found to improve the ductility of polycrystalline Ni_3Al, it does not seem to improve the weldability to the same degree.

To investigate the effect of boron on the weldability of Ni_3Al, a series of welds was made on Ni_3Al with various boron contents (alloys IC-2, 6, 15, 18 and 19). The cracking severity of Ni_3Al is shown as a function of boron content in Fig. 6. The severity of cracking decreased dramatically with the additions of boron up to a level of 200 ppm and increased with further additions of boron. Although boron additions improve grain boundary cohesion, an excess amount of boron may increase the hot cracking tendency of the alloy. Thus the optimum level of boron necessary to ductilize these alloys with good weldability has been found to be about 200 ppm. The alloy containing no boron cracked the most. Also, the cracking behavior of the Ni_3Al containing boron was similar to that of the nickel-iron aluminide (alloy IC-25). The cracking was predominantly in the HAZ.

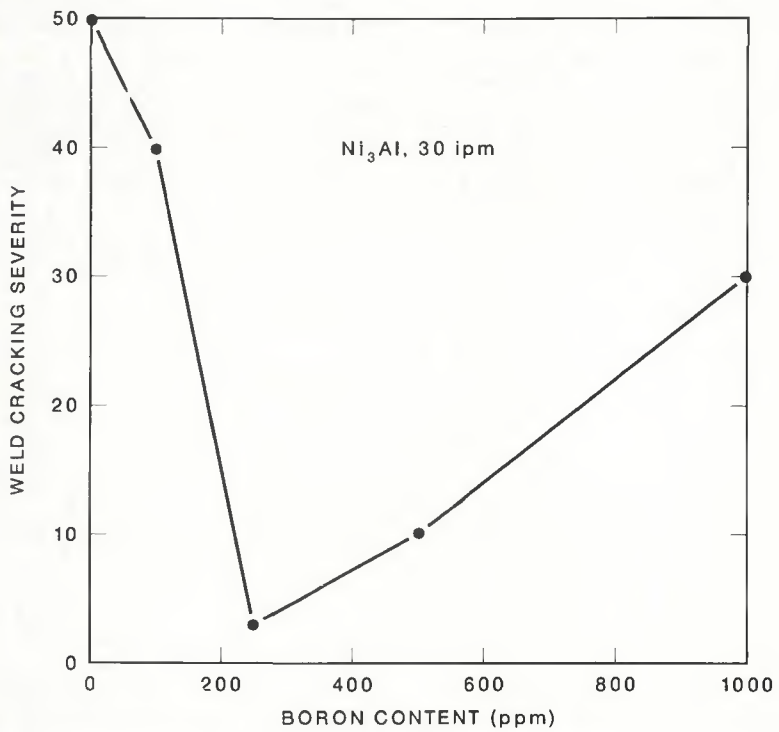

Fig. 6—Weld cracking sensitivity of Ni_3Al as a function of boron content

Boron produces several beneficial effects to the performance of the superalloy family, including improved elevated-temperature strength and improved ductility during fabrication. However, boron has been found to contribute to the conditions that lead to the loss of hot ductility in the HAZ (Ref. 17). This has been shown to be related to localized melting and cracking in the HAZ.

Although boron segregates preferentially to the grain boundaries in boron-doped aluminides (Ref. 5), no such localized melting was observed in the HAZ of the aluminides. However, a ductility minimum at elevated temperatures associated with solute segregation and grain boundary weakness that could lead to cracking is possible. Also the role of a possible contaminant, such as oxygen, in grain boundary embrittlement in this alloy is yet to be identified. The mechanism that controls the hot cracking tendency in nickel aluminides is not fully delineated.

Microstructure

The microstructural features of alloys

Fig. 7—Microstructure showing microcracking tendency of Ni-Fe aluminide during electron beam welding

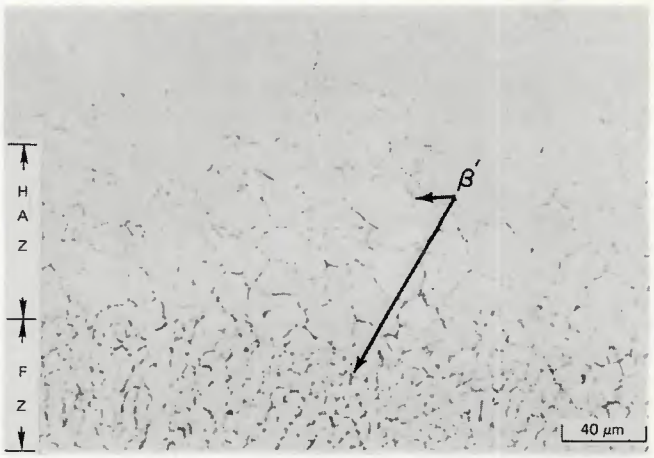

Fig. 8—High magnification showing the presence of β′ in the fusion zone and extensive precipitation of it along the grain boundaries in the HAZ

IC-25 and IC-14 are very similar. Figure 7 shows several microcracks in the fusion zone and the HAZ of an IC-25 EB weld. The fusion zone contains predominantly branched dendritic structure with an interdendritic second phase. Also, significant second-phase precipitation occurs along the boundaries of the HAZ grains during the weld thermal cycle—Fig. 8. The extent of precipitation is directly related to the heat input.

The second phase has been identified as martensitic β' phase. Its origin in the microstructure is related to the weld thermal cycle, and, as discussed earlier, the presence of β' in the fusion zone is due to the aluminum enrichment of the interdendritic liquid during solidification, leading to the formation of β phase (NiAl type) and subsequent transformation of β to a martensitic β' phase due to the rapid cooling during welding. However, in the HAZ, where the specimen is subjected to peak temperatures above the peritectoid temperature, β' will precipitate out as predicted by the phase diagram, leading to a duplex $\gamma + \beta'$ structure.

In both the fusion zone and the HAZ, the presence of martensitic β' represents a nonequilibrium situation as a result of the weld thermal cycle. After homogenizing the weld specimen at 1000°C (1832°F) for 5 h, the β' phase goes into solution as shown in Fig. 9.

A TEM investigation of the alloys IC-25 and IC-14 fusion zone and the HAZ has revealed the presence of antiphase domain boundaries (APB) and martensitic second phase (β') based on the ordered B2 crystal structure. Normally, APB's are not observed in slowly cooled specimens because the ordered domains grow to encompass an entire grain. That APB's are quenched when material is heated to high temperatures but not melted, as in the HAZ, was confirmed by quenching unmelted specimens in water from 1300°C (2372°F) and higher.

The APB's in all specimens exhibited a biomodal distribution of domain sizes. The larger domains, although sometimes unrelated to other microstructural features, were typically next to grain boundaries or the martensitic β' phase. Analysis by EDS showed that these large-domain regions were always enriched in aluminum by about 3 at-% compared with the smaller domains.

A more detailed analysis of this enrichment in rapidly solidified (arc-hammer) Ni_3Al alloys has been presented (Ref. 18). The aluminum enrichment in the welded material, which occurs with and without martensite formation, indicates that sufficient segregation occurs during cooling from elevated temperatures to aid the formation of martensitic phase.

The martensitic phase formed more extensively in the fusion zone than in the HAZ. In the HAZ, the martensite was always in the form of rods or platelets along grain boundaries and at triple points. Figure 10A, a TEM from the HAZ, shows a martensitic β' precipitate along a grain boundary. Figure 10B is a dark-field image using a {110} ordered reflection, which shows APB's in a matrix grain. These domains are small except for those adjacent to the precipitate.

Convergent-beam microdiffraction patterns were used to determine the crystal structure of the martensitic precipitate. The precipitate in Fig. 10 has the CsCl (ordered B2) structure, with approximately 1% tetragonality with $a_0 = 0.290$ nm and $c_0 = 0.292$ nm. Several tetragonal and orthorhombic distortions of the

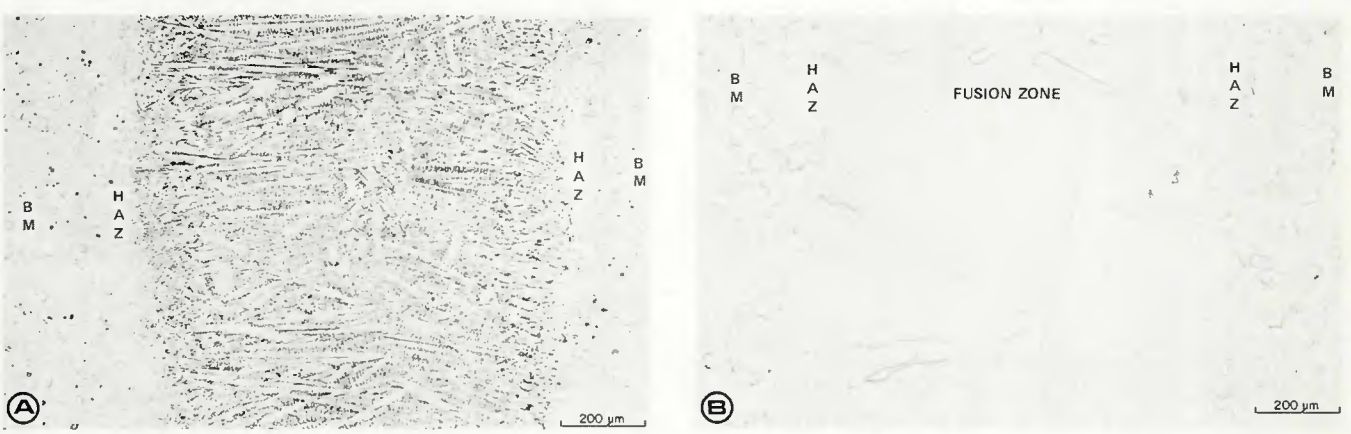

Fig. 9—Photomicrograph of weld showing: A—the presence of interdendritic β′ phase: B—dissolution of β′ after the postweld heat treatment

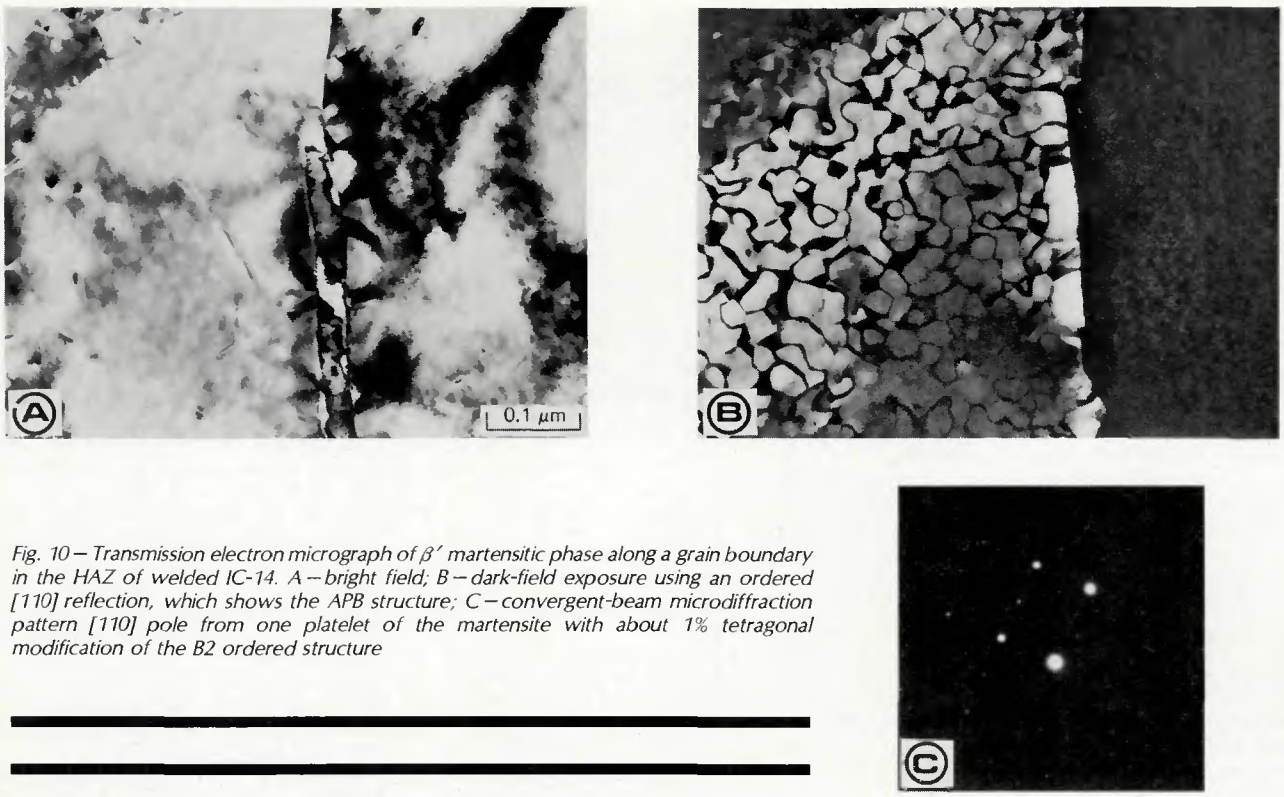

Fig. 10 — Transmission electron micrograph of β′ martensitic phase along a grain boundary in the HAZ of welded IC-14. A — bright field; B — dark-field exposure using an ordered [110] reflection, which shows the APB structure; C — convergent-beam microdiffraction pattern [110] pole from one platelet of the martensite with about 1% tetragonal modification of the B2 ordered structure

body-centered B2 structure have been reported (Refs. 19,20). These lattice parameters are slightly larger than the $a_0 = 0.283$ nm obtained for pure NiAl phase with no added iron.

Compared with the matrix, the composition of this precipitate as determined by EDS analysis showed an aluminum enrichment by 5 at-%, 1 at-% decrease in iron, and 4 at-% decrease in nickel. Regular quenching experiments from temperatures above 1300°C (2372°F) in unmelted specimens also produced similar martensitic second phases.

A TEM of the martensitic phase in the fusion zone is shown in Fig. 11. The β′ phase has been found to have much greater tetragonalities than that in the HAZ, as determined by the diffraction patterns. The greater tetragonality apparently results in more extensive internal twinning of the martensite in the fusion zone, as shown in Fig. 12, than in the HAZ. These precipitates in the fusion zone (Table 2) were slightly more enriched in aluminum than were the precipitates in the HAZ described above.

Table 2—Phase Compositions in Welded IC-14, Wt-%

	Al	Fe	Ni	Ti	Mn
Second phase	26.5	8.0	63.3	0.5	1.5
Matrix	18.8	10.5	69.5	0.3	0.8
Nominal	19.0	10.0	69.5	0.5	1.0

Fig. 11 — Interdendritic β′ phase in the fusion zone

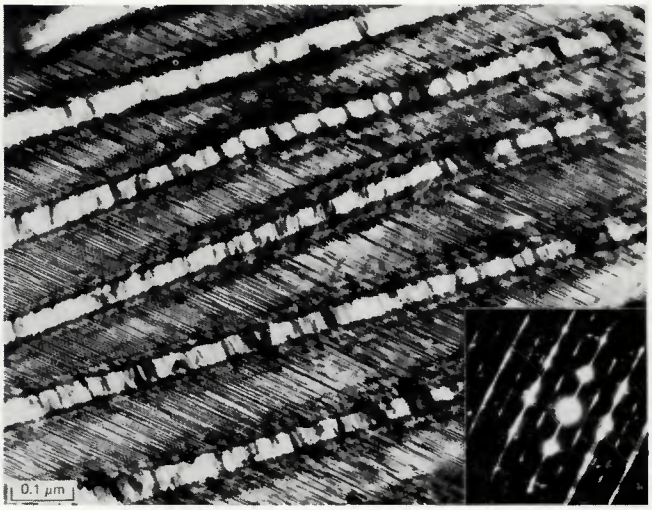

Fig. 12 — Transmission electron micrograph of the β′ martensitic phase in the fusion zone showing extensive internal twinning

Conclusions

The ductile aluminides—in particular, the iron-nickel aluminide—have been found to be prone to cracking during welding. However, the alloy can be EB welded successfully over a narrow range of welding speeds and focus conditions. Boron content and welding speed affect the weldability of this class of material. Although boron is known to greatly improve the ductility of polycrystalline aluminides, it does not seem to improve the weldability significantly.

The observed hot cracking during welding of the aluminides was predominantly in the HAZ and was always intergranular. However, occasional cracking within the fusion zone was also observed. Although cracking observed in this class of material appears to be similar to that in the nickel-base superalloys containing boron, no localized melting was observed. The hot cracking mechanism in this alloy system is not fully delineated.

The weld metal microstructure was duplex, with about 5 to 7 vol-% second phase identified as martensitic β' (NiAl). The formation of this phase is associated with the partitioning of aluminum to the interdendritic liquid during solidification. Also, significant β' precipitate and subsequent transformation to martensitic phase occurs along the grain boundaries in the HAZ. This second phase can be completely eliminated in the weldment by suitable postweld heat treatment.

Acknowledgments

The authors gratefully acknowledge the encouragement of R. A. Bradley and A. C. Schaffhauser as program managers. The authors wish to thank M. L. Santella and W. C. Oliver for reviewing the manuscript and K. Gardner for typing the manuscript. This research was sponsored by the U.S. Department of Energy AR&TD Fossil Energy Materials Program (DOE/FE AA 15 10 10 0, WBS Element ORNL-3.1) and Conservation Energy Conversion and Utilization Technologies Program (EG-05 00 00 0), under contract DE-AC05-840R21400 with the Martin Marietta Energy Systems, Inc.

References

1. Aitken, E. A. 1967. *Intermetallic compounds,* H. H. Westbrook, ed., pp. 491-515. New York.

2. Stoloff, N. S., and Davis, R. G. 1966. The mechanical properties of ordered alloys, *Prog. Mater. Sci.* 13(1): 1-34.

3. Kear, B. H., Sims, C. T., Stoloff, N. S., and Westbrook, J. H., eds. 1970. *Ordered alloys—structural applications and physical metallurgy,* Proc. 3rd Bolton Landing Conf., September, 1969. Baton Rouge, La.: Claitor's Publishing Division.

4. Lipsitt, H. A., Shechtman, D., and Schafrik, R. E. 1980. The deformation and fracture of Ti_3Al at elevated temperatures. *Metall. Trans. A* 11A: 1369.

5. Liu, C. T., White, C. L., Koch, C. C., and Lee, E. H. 1983. Preparation of ductile nickel aluminides for high temperature use. In *Proceedings of the Symposium on High Temperature Materials Chemistry—II,* pp. 32-41, held in San Francisco, May 8-13, 1983, Z. A. Munir and D. Cubicciotti, eds. proc. vol. 83-87, The Electrochemical Society, Pennington, NJ.

6. Aoki, K., and Izumi, O. 1979. Improvement in room temperature ductility of the $L1_2$ type intermetallic compound Ni_3Al by boron addition. *Nippon Kinzaku Gakkaishi* 43: 1190.

7. Zaluzec, N. J. 1979. Quantitative x-ray microanalysis instrumental considerations and applications to materials science. *Introduction to analytical electron microscopy,* J. J. Hren, J. I. Goldstein, and D. C. Joy, eds., pp. 121-167. New York: Plenum Press.

8. American Society for Metals. 1973. Metallography, structure and phase diagrams. *Metals handbook,* vol. 8, 8th ed., p. 262.

9. Rivlin, V. G., and Raynor, G. V. 1980. Critical evaluation of constitution of aluminum-iron-nickel system. *Int. Met. Rev.* 3: 79-93.

10. Liu, C. T., Jemian, W. A., Inouye, H., Cathcart, J. V., David, S. A., Horton, J. A., and Santella, M. L. 1984 (August). *Initial development of nickel and nickel-iron aluminides for structural uses,* Oak Ridge National Laboratory, TM-6067.

11. Puzak, P. P., Apblett, W. R., and Pellini, W. S. 1956. Hot cracking of stainless steel weldments. *Welding Journal* 35(1): 96-s to 175-s.

12. Apblett, W. R., and Pellini, W. S. 1956. Factors which influence weld hot cracking. *Welding Journal* 35(1): 83-s to 90-s.

13. Borland, J. C. 1960. Generalized theory of super-solidus cracking in welds (and castings). *Br. Weld. J.* 7: 558-559.

14. Hull, F. C. 1967. Effect of delta ferrite on the hot cracking of stainless steel. *Welding Journal* 46(8): 399-s to 409-s.

15. David, S. A., and Liu, C. T. 1980 (March). Weldability and hot cracking in thorium-doped iridium alloys. *Met. Technol.* (London) 7: 102-106.

16. Owczarski, W. A. 1969. Effects of minor elements on the weldability of high-nickel alloys. In *Symposium Proceedings, Welding Research Council,* p. 6.

17. Owczarski, W. A., Duvall, D. S., and Sullivan, C. P. 1966. A model for heat-affected zone cracking in nickel-base superalloys. *Welding Journal* 45(4): 145-s to 153-s.

18. Horton, J. A., Koch, C. C., and Liu, C. T. 1983. Segregation and domain structure in rapidly solidified Ni_3Al. *Proceedings of 41st Annual Meeting of the Electron Microscopy Society of America,* pp. 248-249. San Francisco Press.

19. Moskovic, R. 1977. Phase transformations occurring in Ni-rich NiAl during quenching. *J. Mater. Sci.* 12: 489-493.

20. Rosen, S., and Goebel, J. A. 1968. The crystal structure of nickel rich NiAl and martensitic NiAl. *Trans. Metall. Soc./AIME* 242: 722-724.

WRC Bulletin 297
August 1984

Local Stresses in Cylindrical Shells Due to External Loadings on Nozzles—Supplement to WRC Bulletin No. 107

By J. L. Mershon, K. Mokhtarian, G. V. Ranjan, and E. C. Rodabaugh

This document gives methods and data for treating two normally intersecting cylindrical shells. For example, cylindrical nozzles radially attached to cylindrical vessels (shells) are featured. Stresses in both the nozzle and vessel can be determined, and the range of vessel diameter-to-thickness ratio covered is increased over that of Bulletin 107. The analytical method used was derived and developed by C. R. Steele of Shelltech on the basis of thin shell theory.

Publication of this report was sponsored by the Subcommittee on Reinforced Openings and External Loadings of the Pressure Vessel Research Committee of the Welding Research Council. The price of WRC Bulletin 297 is $16.50 per copy, plus $5.00 for postage and handling. Orders should be sent with payment to the Welding Research Council, Room 1301, 345 E. 47 St., New York, NY 10017.